ACS APPLIED MATERIALS & INTERFACES

Research Article

Cite This: ACS Appl. Mater. Interfaces 2019, 11, 43473−43479

www.acsami.org

Energy-Efficient Artificial Synapses Based on Oxide Tunnel Junctions

Jiankun Li,[†] Chen Ge,[*,†,‡] Haotian Lu,[§] Haizhong Guo,[∥] Er-Jia Guo,[†,⊥] Meng He,[†] Can Wang,[†,‡,#] Guozhen Yang,[†] and Kuijuan Jin[†,‡,#]

[†]Beijing National Laboratory for Condensed Matter Physics, Institute of Physics, Chinese Academy of Sciences, Beijing 100190, China

[‡]School of Physical Sciences, University of Chinese Academy of Science, Beijing 100049, China

[§]Department of Electrical and Computer Engineering, University of Illinois, Urbana-Champaign 61820, Illinois, United States

[∥]School of Physical Engineering, Zhengzhou University, Zhengzhou, Henan 450001, China

[⊥]Center of Materials Science and Optoelectronics Engineering, University of Chinese Academy of Sciences, Beijing 100049, China

[#]Songshan Lake Materials Laboratory, Dongguan, Guangdong 523808, China

Supporting Information

ABSTRACT: The development of artificial synapses has enabled the establishment of brain-inspired computing systems, which provides a promising approach for overcoming the inherent limitations of current computer systems. The two-terminal memristors that faithfully mimic the function of biological synapses have intensive prospects in the neural network field. Here, we propose a high-performance artificial synapse based on oxide tunnel junctions with oxygen vacancy migration. Both short-term and long-term plasticities are mimicked in one device. The oxygen vacancy migration through oxide ultrathin films is utilized to manipulate long-term plasticity. Essential synaptic functions, such as paired pulse facilitation, post-tetanic potentiation, as well as spike-timing-dependent plasticity, are successfully implemented in one device by finely modifying the shape of the pre- and postsynaptic spikes. Ultralow femtojoule energy consumption comparable to that of the human brain indicates its potential application in efficient neuromorphic computing. Oxide tunnel junctions proposed in this work provide an alternative approach for realizing energy-efficient brain-like chips.

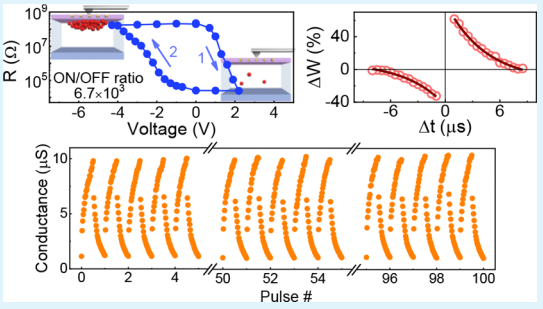

KEYWORDS: *artificial synapses, oxide tunnel junction, synaptic plasticity, oxygen vacancy, pulsed laser deposition*

1. INTRODUCTION

The explosive development of intelligent technologies and systems, such as artificial intelligence, big data, autonomous vehicle, and image/voice recognition, has a dramatic influence on our everyday work and life and also puts forward higher demands for the speed and energy cost of the calculation process.[1−3] However, the improvement of classical computing architectures is limited by a bottleneck associated with the data transfer between the memory and central processing unit, which is commonly called the von Neumann bottleneck.[4] A possible approach to improve the computing performance in intelligent tasks is to store and process the information simultaneously, which is inspired by the operation principle of the human brain.[5,6] Neurologically, massive parallel operation and simultaneous calculation and storage are achieved with 10^{11} neurons and 10^{15} interconnecting synapses (Figure 1a).[7] During the learning and adaptability processes, synapses play a crucial role by reconfiguring their connection strength between two linked neurons, which is called synaptic plasticity. Therefore, implementing the fundamental functions of synaptic plasticity into hardware is an important direction for the realization of artificial neural networks and brain-like chips.[8−12]

Two-terminal memristors with multiple nonvolatile intermediate conductance states have similar structures and transport properties as biological synapses. The basic functions of a biological synapse, such as short-term memory (STM), paired pulse facilitation (PPF), post-tetanic potentiation (PTP), long-term potentiation and depression (LTP/D), and spike-timing-dependent plasticity (STDP), can be emulated by a single memristor.[13] Various types of memristors, such as ferroelectric tunnel junctions,[14−16] conductive filament memories,[17−19] phase change memories,[20] and ion migration-based resistive switching memories,[21−23] have been proposed as promising candidates for performing artificial synaptic behaviors and neural network operations. In most oxide memristors, oxygen vacancy migration is responsible for the resistive switching phenomena.[24] Hussein et al. reported that donor doping in an amorphous $SrTiO_3$ (STO) thin film (~300

Received: July 29, 2019
Accepted: October 15, 2019
Published: November 8, 2019

DOI: 10.1021/acsami.9b13434
ACS Appl. Mater. Interfaces 2019, 11, 43473−43479

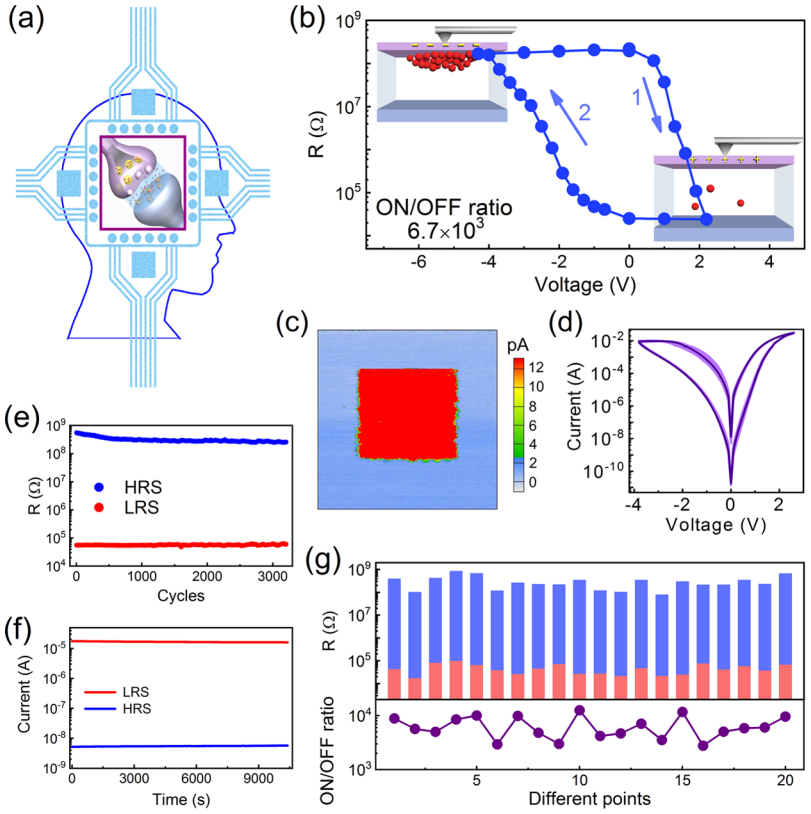

Figure 1. Voltage control of OTJs. (a) Schematic diagram of an artificial synapse. (b) Typical resistance hysteresis loop of an OTJ. The pristine device state is the HRS, and the loop direction is indicated by arrows. The junction resistance is measured at V_{read} 0.1 V after the application of V_{write} with different amplitudes (~100 ms). The oxygen vacancy positions of the LRS and HRS are shown schematically in the top-left and bottom-right insets, respectively. (c) Current mapping acquired by C-AFM over an area of 5 × 5 μm^2 with the opposite write voltages. The pattern was written by ±6.5 V and the current mapping was read by +0.5 V. (d) Current−voltage (I−V) loops for 200 cycles. (e) Fatigue property at the ON/OFF ratio of 5 × 10^3 for more than 3 × 10^3 cycles. The write voltages are −4.3 V for the HRS and +2.2 V for the LRS, respectively. (f) Retention property of an OTJ device up to more than 10^4 s. (g) Uniformity of the device resistance. The HRS (blue) and LRS (magenta) resistances of 20 different devices are shown (upper panel), with the corresponding ON/OFF ratios in the lower panel.

nm) could improve the performance of memristive nanodevices for low energy and multilevel operation.[25] The thickness of oxide films is typically much larger than 10 nm. When the thickness of the oxide films is reduced to several nanometers, the voltage required to drive the oxygen vacancies will be lowered, and the distance that the oxygen vacancies need to pass will be decreased, which will dramatically shorten the resistance switching time and reduce the energy consumption.

In this work, oxide tunnel junctions (OTJs) based on oxide ultrathin films, by utilizing an ionic degree of freedom, are introduced for neuromorphic computing. In the OTJs, quantum-mechanical tunneling dominates at a low resistance state (LRS), and the thermionic emission (TE) mechanism plays a key role at a high resistance state (HRS). The conduction mechanism can be electrically switched by the oxygen vacancy migration. The simple structure, long retention, and good switching reproducibility of the OTJs make them a promising candidate for biological synapses. Essential synaptic functions, such as STP, PPF, PTP, LTP/D, and STDP, are implemented in a single device. These results may promote the applications of OTJs in neuromorphic devices.

2. EXPERIMENTAL SECTION

2.1. Device Fabrication. STO epitaxial films with a thickness of ~2.8 nm were grown by pulsed laser deposition (PLD) on (001)-oriented Nb-doped STO (SNTO) single-crystalline substrates (0.7 wt %), which served as the bottom electrodes. The thickness of STO ultrathin films was confirmed by X-ray reflection and scanning transmission electron microscopy measurements of $BaTiO_3$ ultrathin films deposited under the same condition.[26] A XeCl excimer laser is used with a wavelength of 308 nm and a repetition rate of 2 Hz. The STO films were deposited at 750 °C in a flowing oxygen atmosphere of 1 Pa. Circular platinum electrodes with a radius of 10 μm and a thickness of 100 nm were patterned by photolithography and e-beam evaporation followed by a lift-off process.

2.2. Electrical Measurement and Characterization. Conductive atomic force microscopy (C-AFM) measurements were performed using a commercial scanning probe microscope (Asylum Research MFP3D). Conductive diamond-coated silicon tips were employed with a written voltage of ±7 V and a read voltage of +0.5 V. During the measurement of electrical properties, the OTJ sample is placed in a LakeShore TTPX probe station with 3 μm W probes. A Keithley 4200 semiconductor characterization system with 4225-PMU Ultra-Fast IV Modules is connected to the probe station to apply the test pulses. Positive bias means that the currents flow from the Pt electrodes to the SNTO substrates, and the SNTO substrates were always grounded.

DOI: 10.1021/acsami.9b13434
ACS Appl. Mater. Interfaces 2019, 11, 43473−43479

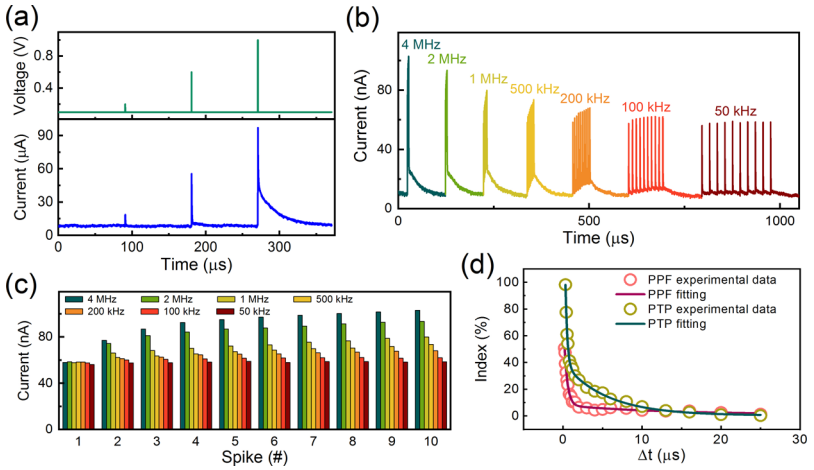

Figure 2. Short-term plasticity emulated in OTJs. (a) Instantaneous response current triggered by the small presynaptic spikes. The applied voltage consists of a series of programming voltages with the same duration of 50 ns and different amplitudes of 0.2, 0.6, and 1 V. (b) EPSCs corresponding to the STM stimulus with different trigger frequencies. The pulse amplitude is 0.6 V and the pulse width is 50 ns. (c) Peak currents as a function of stimulation number and frequency summarized from (b). (d) PPF and PTP characteristics of OTJs. The experimental data are expressed by the hollow circles, and the fitting results are expressed by the solid curves.

3. RESULTS AND DISCUSSION

A three-layer structure composed of an ultrathin oxide film and two conductive electrodes was fabricated as a biological synapse. In this study, single crystalline SNTO substrates were used as substrates and bottom electrodes. The epitaxial STO ultrathin films with a thickness of 2.8 nm were deposited by PLD. Then, the Pt top electrodes were patterned on the STO/SNTO heterostructure using the standard lithography technique.

Through adjusting the migration of oxygen vacancies by applying an external electric field with various amplitudes, a clear nonvolatile resistance−voltage ($R-V$) hysteresis loop appeared in the OTJs (Figure 1b). The testing pulse train was composed of write pulses with a duration of ∼100 ms and read pulses following each write pulse. When the write voltage (V_{write}) was swept between −4.3 and +2.2 V, the ON/OFF ratio between the HRS (1.8×10^8 Ω) and the LRS (2.7×10^4 Ω) reached the value as high as 6.7×10^3. An extensive range of the intermediate resistance states was observed in the $R-V$ loop, which denoted the gradual switching between the LRS and HRS. As shown in Figure 1b, when a negative V_{write} was applied to the top electrode, the positively charged oxygen vacancies moved toward the top electrode. Then, the HRS was formed, which was also the pristine resistance state for all the OTJs. The $I-V$ curve at the HRS showed an obvious asymmetry. We demonstrated that the TE model was responsible for the conduction mechanism based on our fitting results (Figure S1a, Supporting Information).[26] The extracted Schottky barrier height Φ_B of 0.55 eV was acquired by fitting the $I-V$ curve with the exponential function. In contrast, when the negative V_{write} was reversed to the positive voltage, the oxygen vacancies moved away from the top electrode, and LRS was produced. The local $I-V$ curve at the LRS showed a tunneling behavior, which was further confirmed by fitting the curve with the direct tunnel (DT) model and the Fowler−Nordheim tunneling (FNT) model (Figure S1b, Supporting Information). The DT barrier heights at the Pt/STO and STO/SNTO interfaces were 0.35 and 0.41 eV, respectively, and the FNT barrier height was 0.075 eV. More calculation details could be found in Note S1 in the Supporting Information.

To characterize the voltage-dependent resistance states on the microscale, C-AFM measurements were conducted by using two opposite voltages (Figure 1c). The pattern was written by applying an external voltage of −6.5 V to a square of 5×5 μm^2 and +6.5 V to a square of 2.5×2.5 μm^2 inside it. A dc bias of +0.5 V was applied to acquire the resistance mapping properties. In agreement with the $R-V$ results, the current of the inner domain exhibited a larger value. On the contrary, the outer area written by a negative voltage remains at HRS. This means that positive voltages induce the LRS, consistent with the patterned device measurements.

We investigated the reliability performance of the OTJ devices. An $I-V$ hysteresis loop for 200 cycles with high reproducibility was obtained (Figure 1d). The asymmetry of the $R-V$ and $I-V$ loops was ascribed to the difference between the top and bottom electrodes. The ON/OFF ratio of the OTJ could be maintained at about 5×10^3 after switching between the HRS and LRS for more than 3000 cycles (Figure 1e), suggesting the good switchability property. Moreover, the retention test of the HRS and LRS was performed for more than 10^4 s, indicating a good nonvolatility (Figure 1f). Therefore, we tested the resistance values of 20 different devices, indicating a good uniformity (Figure 1g). Here, V_{write} was −4.3 V for the HRS and +2.2 V for the LRS, and the read voltage (V_{read}) was +0.1 V.

Human brain constantly accepts and processes complicated information. Neurobiologically, this information is transmitted as an electrical signal between the synapses, which causes a change in the strength of the synaptic connection, called as synaptic plasticity. Synaptic plasticity, consisting of STM and long-term memory (LTM), is the basis for information processing and memory formation in the human brain.[27,28] In our OTJs, synaptic plasticity of both STM and LTM characteristics can be emulated through the use of input pulse amplitude and duration. STM can be achieved using voltages less than the threshold value (Figure 2a). When a presynaptic pulse is applied, the excitatory postsynaptic current (EPSC) rises immediately and then gradually decreases to the resting value. STM is capacitive in nature.[29] Therefore, the relaxation

DOI: 10.1021/acsami.9b13434
ACS Appl. Mater. Interfaces 2019, 11, 43473−43479

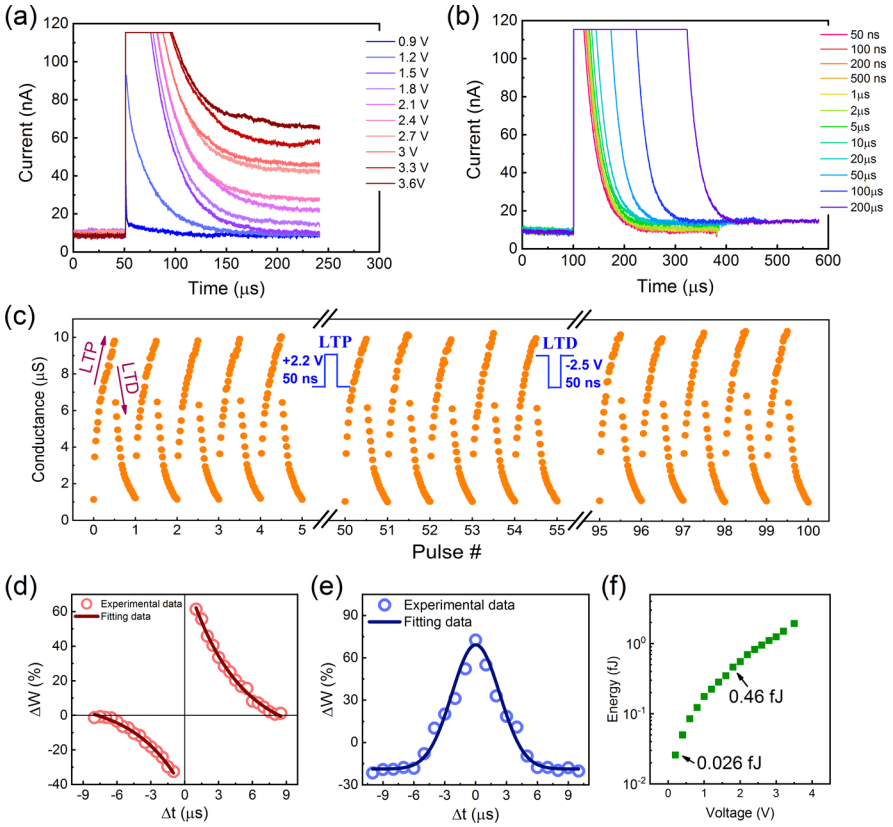

Figure 3. (a) Currents stimulated by the presynaptic spikes with different amplitudes and the same duration of 100 ns. The current compliance is 115 nA. (b) Dependence of the device conductance on the spike duration. The spike amplitude is 1.5 V. The current compliance is 115 nA. (c) 20 LTP/D conductance states for 100 cycles obtained by alternating positive (+2.2 V) and negative (−2.5 V) pulse trains. (d,e) Implementation of STDP learning in OTJ devices. Antisymmetric (d) and symmetric (e) Hebbian learning rules are realized in one device. The solid fitting lines are calculated by eqs 1 and 2. (f) Energy consumption per spike as a function of the presynaptic pulse amplitude.

process of the OTJ-based artificial synapses can be described by an exponential decay function, $I = I_0 \exp(-t/\tau_1)$, where R_0 is the circuit resistance, and τ_1 is the relaxation time constant which is closely related to the forgetting rate.[30] The fitting results to the decay curves and related parameters are shown in Figure S2, Supporting Information. Figure 2b shows the EPSC triggered by presynaptic pulses with different frequencies in the STM mode. The stimulus consisted of 10 identical pulses with a voltage of 0.6 V and a pulse width of 50 ns. To clearly show the changes in the EPSC peak at different frequencies, the EPSC peak versus stimulation number is demonstrated in Figure 2c. When the pulse frequency increased, the peak value also increased because of the influence of the previous pulse.

The temporary enhancement of the EPSC provides the basis for the OTJ device to simulate the PPF and PTP characteristics in biological synapses. PPF and PTP, the two forms of the most well-known STM phenomena, depict the temporary boost of synaptic weight evoked by the second and the 10th pulse, respectively. In an OTJ device, successive stimuli with the pulse intervals that are comparable or shorter than the relaxation time can be utilized to simulate the PPF and PTP phenomena (Figure 2d). The PPF and PTP responses as the functions of time interval (Δt) were measured using a spike amplitude of 0.6 V and a spike duration of 50 ns (Figure S3, Supporting Information). The indexes of PPF $[(A_2 - A_1)/A_1$ ratio given in %] and PTP $[(A_{10} - A_1)/A_1$ ratio given in %] decreased almost exponentially as Δt increased, similar to the response of biological synapses.[31]

LTM, containing LTP and LTD, is essential for implementing the brain-like computation in artificial synapses.[27] In OTJ devices, STM can be transited to LTM by varying different parameters. The conductance of an OTJ device is adjusted successfully by nanosecond pulse with different amplitudes (Figure 3a). By increasing the spike amplitude (from 0.9 to 3.6 V), the obtained channel currents decayed to the stable values that were larger than the initial value after each spike (from 8.5 to 65.5 nA). The corresponding conductance changes with the spike amplitude are shown in Figure S4 in the Supporting Information. The transition from STM to LTM can also be realized by increasing the width of the presynaptic spikes. Figure 3b illustrates the EPSCs obtained by applying the stimuli with different widths. The pulse amplitude was fixed to 1.5 V. The training results show an obvious potentiation of the conductance as the pulse width increased, and all the EPSCs finally reached a saturated value (Figure S5, Supporting Information) by alternately applying a series of 20 identical pulses (+2.2 and −2.5 V, 50 ns) for 100 cycles. Switching between the LTP and LTD in the OTJ device was obtained at a conductance between 1 and 10.5 μS (Figure 3c). The conductance in both rising and falling processes was set to 20 intermediate states.

By combining the characteristics of the STM and LTM, complicated forms of memory behavior, for example, STDP, can be employed to achieve complex synaptic functions. As the Hebbian model shows,[32] STDP is defined as a synaptic modification arising from the precise relative timing of fired

DOI: 10.1021/acsami.9b13434
ACS Appl. Mater. Interfaces 2019, 11, 43473−43479

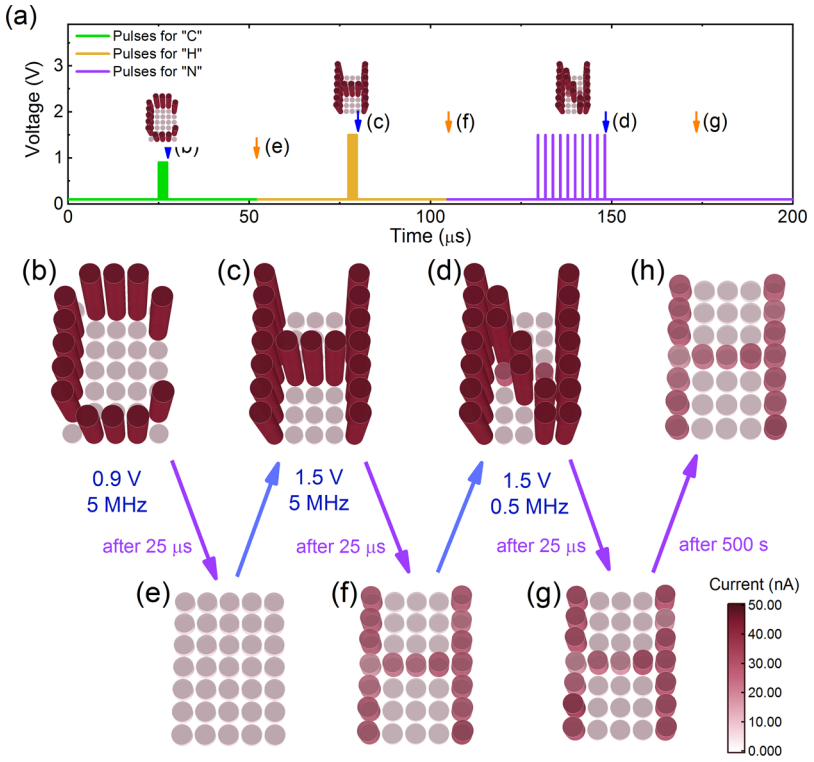

Figure 4. Image memorization in an artificial synapse array. (a) Three types of pulse sequences represented by the letters "C" (the short-term potentiation mode), "H" (the long-term potentiation mode), and "N" (the short-term potentiation mode). Ten consecutive stimulus pulses with the duration of 50 ns, amplitude of 0.9 and 1.5 V, and pulse frequency of 5 and 0.5 MHz are input into the synapse array. (b–d) Images "C", "H", and "N" just after the last pulse [blue arrows in (a)]. (e–g) Images "C", "H", and "N", 25 μs after the last pulse [orange arrows in (a)]. The read voltage of 0.1 V was used here. (h) Retention property of the letter "H" up to 500 s.

spikes of connected neurons. STDP plays an important role in information processing, associated with learning and neural network functions.[33,34] To demonstrate the conductance modulation of STDP functionality in OTJ devices, various STDP forms were implemented by adopting typical strategies used in biological synapses and electronic synapses.[35]

In the antisymmetric Hebbian learning STDP form, the sign and magnitude of a synaptic weight depend on the relative time sequence and interval of the pre- and postsynaptic spike sequences (Δt). Both the pre- and postsynaptic sequences consist of a series of progressively increasing negative pulses and a large positive pulse with a duration of 1 μs (Figure S6, Supporting Information). Here, the voltage of both presynaptic spikes (V_{pre}) and postsynaptic spikes (V_{post}) is less than the threshold voltage of $\pm$1.5 V. When the presynaptic spikes are triggered preceding the postsynaptic spikes ($\Delta t > 0$), the synaptic weight is strengthened, and LTP occurs. On the other hand, when the order is reversed ($\Delta t < 0$), LTD occurs (Figure 3d). Thus, the law of antisymmetric Hebbian learning STDP form can be expressed by an exponential function[36,37]

$$\Delta W = A \exp\left(\frac{-\Delta t}{\tau_2}\right) + W_0 \quad (1)$$

where ΔW denotes the nonvolatile percent change of synaptic weight, A denotes the scaling factor, τ_2 denotes the time constant, and W_0 denotes a constant. In the OTJ test, A of 96.3 and τ_2 of 4.4 μs were used in the LTP branch, and A of −53.1 and τ_2 of −4.2 μs were used in the LTD branch. The fitting results are demonstrated by the solid curves (Figure 3d). When the absolute value of Δt decreased, the maximum absolute value of $V_{pre} - V_{post}$ increased. This results in the strengthening or weakening of the device conductance, depending on the sign of Δt.

The symmetric Hebbian learning STDP form can also be realized in OTJs by selecting the appropriate shapes of pre- and postsynaptic spikes (Figures 3e and S7, Supporting Information). LTP occurs when Δt was close to 0, and LTD occurs when Δt moves away from 0.[38] The characteristics of the symmetric Hebbian learning STDP form can be generalized by a Gaussian function

$$\Delta W = A \exp\left(\frac{-\Delta t^2}{\tau_3^2}\right) + W_0 \quad (2)$$

In the fitting curve presented in Figure 3e, A = 88.0 and τ_3 = 3.3 μs. The STDP forms in OTJs are 4 orders of magnitude faster than those in the human brain.

We estimated the energy consumption of our OTJs. We initialized the resistance state and measured the EPSCs by applying 20 ns pulses of different pulse amplitudes. We find that, with the pulse width of 20 ns, STM becomes LTM if the pulse amplitude exceeds the threshold voltage of 1.8 V. The energy consumption can be calculated by $E = V \times I \times t$, where V, I, and t represent the pulse amplitude, the current (20 ns), and the pulse width, respectively. Therefore, the energy consumptions of STM and LTM are respectively 0.026 and 0.46 fJ, comparable with that of human synapses (1–10 fJ) (Figure 3f). These values are favorable compared with other two-terminal artificial synapses (hundreds of femtojoules for 0.1 μm^2).[14,15,39]

DOI: 10.1021/acsami.9b13434
ACS Appl. Mater. Interfaces 2019, 11, 43473–43479

To further illustrate the coexistence of both STM and LTM, a synapse array consisting of 25 individual OTJs was employed to implement the reconfigurable and trainable memory behavior. This experiment also mimicked the selective activation in the parietal cortex. Three letters were successively input into the selected individual pixels: (1) the letter "C" in the STM mode (10 stimuli with a low amplitude of 0.9 V and a high frequency of 5 MHz); (2) the letter "H" in the LTM mode (10 stimuli with a high amplitude of 1.5 V and a high frequency of 5 MHz); and (3) the letter "N" in the STM mode (10 stimuli with a high amplitude of 1.5 V and a low frequency of 0.5 MHz) (Figure 4a). The pulse duration was fixed at 50 ns, and the read voltage was fixed at 0.1 V. All pixels were initialized to the HRS before the electrical stimuli. The pixel resistances were read individually at the end of the training process (blue arrows) and 25 μs later (orange arrows), respectively. To intuitively illustrate the memorization and forgetting process, the memorized patterns at these moments, indicated by blue and orange arrows, are depicted in Figure 4b–g. After training with the three letters, the current of each corresponding pixel exhibited a temporary enhancement (Figure 4b–d). As time passed, the currents representing the letters "C" and "N" gradually disappeared (Figure 4e,g). In contrast, the excitatory currents of pixels corresponding to the letter "H" were maintained because of the LTM nature (Figure 4f). The letter "H" showed good stability and remained unchanged for more than 500 s (Figure 4h). This process is similar with the memory behavior in the human brain.

4. CONCLUSIONS

In summary, we presented robust artificial synapses based on OTJs with the oxygen vacancy migration. The energy consumption of the two-terminal device is reduced to an ultralow level of femtojoules by exploiting an ultrathin oxide layer. Our experimental results provide evidence for various types of important synaptic functions such as STM, PPF, PTP, LTP, and LTD. By finely tuning the shape of the pre- and postsynaptic spikes, antisymmetric and symmetric Hebbian learning STDP forms are realized. Our artificial synapse based on OTJs represents a promising approach for energy-efficient brain-like computing.

■ ASSOCIATED CONTENT

Supporting Information

The Supporting Information is available free of charge on the ACS Publications website at DOI: 10.1021/acsami.9b13434.

Complete analysis of HRS and LRS, complete study of STM, variation of conductance induced by presynaptic pulses with different amplitudes and widths, and waveform of STDP (PDF)

■ AUTHOR INFORMATION

Corresponding Author

*E-mail: gechen@iphy.ac.cn.

ORCID

Chen Ge: 0000-0002-8093-940X

Can Wang: 0000-0002-4404-7957

Kuijuan Jin: 0000-0002-0047-4375

Author Contributions

C.G. conceived and designed the experiments. K.J. directed the project. J.L. fabricated samples and carried out the device measurements under the supervision of C.G. J.L. and C.G. wrote the manuscript. All authors commented on the manuscript.

Notes

The authors declare no competing financial interest.

■ ACKNOWLEDGMENTS

This work was supported by the National Key R&D Program of China (no. 2017YFA0303604), the National Natural Science Foundation of China (nos. 11674385, 11404380, 11721404, and 11874412), the Youth Innovation Promotion Association of CAS (no. 2018008), and the Key Research Program of Frontier Sciences CAS (no. QYZDJSSW-SLH020).

■ ABBREVIATIONS

STM, short-term memory
PPF, paired pulse facilitation
PTP, post-tetanic potentiation
LTP/D, long-term potentiation and depression
STDP, spike-timing-dependent plasticity
FTJ, ferroelectric tunnel junction
PCM, phase change memories
OTJ, oxide tunnel junction
TE, thermionic emission mechanism
L/HRS, low/high resistance state
STO, $SrTiO_3$
PLD, pulse laser deposition
SNTO, Nb-doped $SrTiO_3$
C-AFM, conductive atomic force microscopy
DT, direct tunnel
FNT, Fowler–Nordheim tunneling
EPSC, excitatory postsynaptic current

■ REFERENCES

(1) Xia, Q.; Yang, J. J. Memristive Crossbar Arrays for Brain-Inspired Computing. *Nat. Mater.* **2019**, *18*, 309–323.

(2) Zidan, M. A.; Strachan, J. P.; Lu, W. D. The Future of Electronics Based on Memristive Systems. *Nat. Electron.* **2018**, *1*, 22–29.

(3) LeCun, Y.; Bengio, Y.; Hinton, G. Deep Learning. *Nature* **2015**, *521*, 436–444.

(4) Huang, W.; Fang, Y.-W.; Yin, Y.; Tian, B.; Zhao, W.; Hou, C.; Ma, C.; Li, Q.; Tsymbal, E. Y.; Duan, C.-G.; Li, X. Solid-State Synapse Based on Magnetoelectrically Coupled Memristor. *ACS Appl. Mater. Interfaces* **2018**, *10*, 5649–5656.

(5) Ge, C.; Liu, C.-X.; Zhou, Q.-L.; Zhang, Q.-H.; Du, J.-Y.; Li, J.-K.; Wang, C.; Gu, L.; Yang, G.-Z.; Jin, K.-J. A Ferrite Synaptic Transistor with Topotactic Transformation. *Adv. Mater.* **2019**, *31*, No. e1900379.

(6) Wang, Y.; Zhang, Z.; Xu, M.; Yang, Y.; Ma, M.; Li, H.; Pei, J.; Shi, L. Self-Doping Memristors with Equivalently Synaptic Ion Dynamics for Neuromorphic Computing. *ACS Appl. Mater. Interfaces* **2019**, *11*, 24230–24240.

(7) Yang, J.-T.; Ge, C.; Du, J.-Y.; Huang, H.-Y.; He, M.; Wang, C.; Lu, H.-B.; Yang, G.-Z.; Jin, K.-J. Artificial Synapses Emulated by an Electrolyte-Gated Tungsten-Oxide Transistor. *Adv. Mater.* **2018**, *30*, 1801548.

(8) Zhu, X.; Li, D.; Liang, X.; Lu, W. D. Ionic modulation and ionic coupling effects in MoS_2 devices for neuromorphic computing. *Nat. Mater.* **2019**, *18*, 141–148.

(9) Jordan, M. I.; Mitchell, T. M. Machine Learning: Trends, Perspectives, and Prospects. *Science* **2015**, *349*, 255–260.

(10) Prezioso, M.; Merrikh-Bayat, F.; Hoskins, B. D.; Adam, G. C.; Likharev, K. K.; Strukov, D. B. Training and Operation of an

DOI: 10.1021/acsami.9b13434
ACS Appl. Mater. Interfaces 2019, 11, 43473–43479

Integrated Neuromorphic Network Based on Metal-Oxide Memristors. *Nature* **2015**, *521*, 61−64.
(11) Huang, H.-M.; Yang, R.; Tan, Z. H.; He, H. K.; Zhou, W.; Xiong, J.; Guo, X. Quasi-Hodgkin-Huxley Neurons with Leaky Integrate-and-Fire Functions Physically Realized with Memristive Devices. *Adv. Mater.* **2019**, *31*, 1803849.
(12) Huang, H.-Y.; Ge, C.; Zhang, Q. H.; Liu, C. X.; Du, J. Y.; Li, J. K.; Wang, C.; Gu, L.; Yang, G. Z.; Jin, K. J. Electrolyte-Gated Synaptic Transistor with Oxygen Ions. *Adv. Funct. Mater.* **2019**, *29*, 1902702.
(13) Yang, R.; Huang, H.-M.; Hong, Q.-H.; Yin, X.-B.; Tan, Z.-H.; Shi, T.; Zhou, Y.-X.; Miao, X.-S.; Wang, X.-P.; Mi, S.-B.; Jia, C.-L.; Guo, X. Synaptic Suppression Triplet-STDP Learning Rule Realized in Second-Order Memristors. *Adv. Funct. Mater.* **2018**, *28*, 1704455.
(14) Chanthbouala, A.; Garcia, V.; Cherifi, R. O.; Bouzehouane, K.; Fusil, S.; Moya, X.; Xavier, S.; Yamada, H.; Deranlot, C.; Mathur, N. D.; Bibes, M.; Barthélémy, A.; Grollier, J. A Ferroelectric Memristor. *Nat. Mater.* **2012**, *11*, 860−864.
(15) Boyn, S.; Grollier, J.; Lecerf, G.; Xu, B.; Locatelli, N.; Fusil, S.; Girod, S.; Carrétéro, C.; Garcia, K.; Xavier, S.; Tomas, J.; Bellaiche, L.; Bibes, M.; Barthélémy, A.; Saïghi, S. Learning through Ferroelectric Domain Dynamics in Solid-State Synapses. *Nat. Commun.* **2017**, *8*, 14736.
(16) Guo, R.; Zhou, Y.; Wu, L.; Wang, Z.; Lim, Z.; Yan, X.; Lin, W.; Wang, H.; Yoong, H. Y.; Chen, S.; Ariando; Venkatesan, T.; Wang, J.; Chow, G. M.; Gruverman, A.; Miao, X.; Zhu, Y.; Chen, J. Control of Synaptic Plasticity Learning of Ferroelectric Tunnel Memristor by Nanoscale Interface Engineering. *ACS Appl. Mater. Interfaces* **2018**, *10*, 12862−12869.
(17) Wang, Z.; Joshi, S.; Savel'ev, S.; Song, W.; Midya, R.; Li, Y.; Rao, M.; Yan, P.; Asapu, S.; Zhuo, Y.; Jiang, H.; Lin, P.; Li, C.; Yoon, J. H.; Upadhyay, N. K.; Zhang, J.; Hu, M.; Strachan, J. P.; Barnell, M.; Wu, Q.; Wu, H.; Williams, R. S.; Xia, Q.; Yang, J. J. Fully Memristive Neural Networks for Pattern Classification with Unsupervised Learning. *Nat. Electron.* **2018**, *1*, 137−145.
(18) Choi, S.; Tan, S. H.; Li, Z.; Kim, Y.; Choi, C.; Chen, P.-Y.; Yeon, H.; Yu, S.; Kim, J. SiGe Epitaxial Memory for Neuromorphic Computing with Reproducible High Performance Based on Engineered Dislocations. *Nat. Mater.* **2018**, *17*, 335−340.
(19) Zhou, L.; Mao, J.-Y.; Ren, Y.; Yang, J.-Q.; Zhang, S.-R.; Zhou, Y.; Liao, Q.; Zeng, Y.-J.; Shan, H.; Xu, Z.; Fu, J.; Wang, Y.; Chen, X.; Lv, Z.; Han, S.-T.; Roy, V. A. L. Biological Spiking Synapse Constructed from Solution Processed Bimetal Core-Shell Nanoparticle Based Composites. *Small* **2018**, *14*, 1800288.
(20) Ambrogio, S.; Ciocchini, N.; Laudato, M.; Milo, V.; Pirovano, A.; Fantini, P.; Ielmini, D. Unsupervised Learning by Spike Timing Dependent Plasticity in Phase Change Memory (PCM) Synapses. *Front. Neurosci.* **2016**, *10*, 56.
(21) Fuller, E. J.; Gabaly, F. E.; Léonard, F.; Agarwal, S.; Plimpton, S. J.; Jacobs-Gedrim, R. B.; James, C. D.; Marinella, M. J.; Talin, A. A. Li-Ion Synaptic Transistor for Low Power Analog Computing. *Adv. Mater.* **2017**, *29*, 1604310.
(22) Gao, S.; Liu, G.; Yang, H.; Hu, C.; Chen, Q.; Gong, G.; Xue, W.; Yi, X.; Shang, J.; Li, R.-W. An Oxide Schottky Junction Artificial Optoelectronic Synapse. *ACS Nano* **2019**, *13*, 2634−2642.
(23) Yang, Y.; Zhang, X.; Qin, L.; Zeng, Q.; Qiu, X.; Huang, R. Probing Nanoscale Oxygen Ion Motion in Memristive Systems. *Nat. Commun.* **2017**, *8*, 15173.
(24) Lü, W.; Li, C.; Zheng, L.; Xiao, J.; Lin, W.; Li, Q.; Wang, X. R.; Huang, Z.; Zeng, S.; Han, K.; Zhou, W.; Zeng, K.; Chen, J.; Ariando; Cao, W.; Venkatesan, T. Multi-Nonvolatile State Resistive Switching Arising from Ferroelectricity and Oxygen Vacancy Migration. *Adv. Mater.* **2017**, *29*, 1606165.
(25) Nili, H.; Walia, S.; Kandjani, A. E.; Ramanathan, R.; Gutruf, P.; Ahmed, T.; Balendhran, S.; Bansal, V.; Strukov, D. B.; Kavehei, O.; Bhaskaran, M.; Sriram, S. Donor-Induced Performance Tuning of Amorphous $SrTiO_3$ Memristive Nanodevices: Multistate Resistive Switching and Mechanical Tunability. *Adv. Funct. Mater.* **2015**, *25*, 3172−3182.
(26) Li, J.; Li, N.; Ge, C.; Huang, H.; Sun, Y.; Gao, P.; He, M.; Wang, C.; Yang, G.; Jin, K. Giant Electroresistance in Ferroionic Tunnel Junctions. *iScience* **2019**, *16*, 368−377.
(27) Whitlock, J. R.; Heynen, A. J.; Shuler, M. G.; Bear, M. F. Learning Induces Long-Term Potentiation in the Hippocampus. *Science* **2006**, *313*, 1093−1097.
(28) Bliss, T. V. P.; Collingridge, G. L. A Synaptic Model of Memory: Long-Term Potentiation in the Hippocampus. *Nature* **1993**, *361*, 31−39.
(29) van de Burgt, Y.; Lubberman, E.; Fuller, E. J.; Keene, S. T.; Faria, G. C.; Agarwal, S.; Marinella, M. J.; Alec Talin, A.; Salleo, A. A Non-Volatile Organic Electrochemical Device as a Low-Voltage Artificial Synapse for Neuromorphic Computing. *Nat. Mater.* **2017**, *16*, 414−418.
(30) Hu, L.; Fu, S.; Chen, Y.; Cao, H.; Liang, L.; Zhang, H.; Gao, J.; Wang, J.; Zhuge, F. Ultrasensitive Memristive Synapses Based on Lightly Oxidized Sulfide Films. *Adv. Mater.* **2017**, *29*, 1606927.
(31) Bao, J.-X.; Kandel, E. R.; Hawkins, R. D. Involvement of Pre- and Postsynaptic Mechanisms in Posttetanic Potentiation at Aplysia Synapses. *Science* **1997**, *275*, 969−973.
(32) Hebb, D. O. *The Organization of Behavior: A Neuropsychological Theory*; Wiley, 1949.
(33) Young, J. M.; Waleszczyk, W. J.; Wang, C.; Calford, M. B.; Dreher, B.; Obermayer, K. Cortical reorganization consistent with spike timing-but not correlation-dependent plasticity. *Nat. Neurosci.* **2007**, *10*, 887−895.
(34) Wang, Z.; Joshi, S.; Savel'ev, S. E.; Jiang, H.; Midya, R.; Lin, P.; Hu, M.; Ge, N.; Strachan, J. P.; Li, Z.; Wu, Q.; Barnell, M.; Li, G.-L.; Xin, H. L.; Williams, R. S.; Xia, Q.; Yang, J. J. Memristors with Diffusive Dynamics as Synaptic Emulators for Neuromorphic Computing. *Nat. Mater.* **2017**, *16*, 101−108.
(35) Jang, B. C.; Kim, S.; Yang, S. Y.; Park, J.; Cha, J.-H.; Oh, J.; Choi, J.; Im, S. G.; Dravid, V. P.; Choi, S.-Y. Polymer Analog Memristive Synapse with Atomic-Scale Conductive Filament for Flexible Neuromorphic Computing System. *Nano Lett.* **2019**, *19*, 839−849.
(36) Froemke, R. C.; Dan, Y. Spike-Timing-Dependent Synaptic Modification Induced by Natural Spike Trains. *Nature* **2002**, *416*, 433−438.
(37) Bi, G.-q.; Poo, M.-m. Synaptic Modification by Correlated Activity: Hebb's Postulate Revisited. *Annu. Rev. Neurosci.* **2001**, *24*, 139−166.
(38) John, R. A.; Yantara, N.; Ng, Y. F.; Narasimman, G.; Mosconi, E.; Meggiolaro, D.; Kulkarni, M. R.; Gopalakrishnan, P. K.; Nguyen, C. A.; De Angelis, F.; Mhaisalkar, S. G.; Basu, A.; Mathews, N. Ionotronic Halide Perovskite Drift-Diffusive Synapses for Low-Power Neuromorphic Computation. *Adv. Mater.* **2018**, *30*, 1805454.
(39) Shi, Y.; Liang, X.; Yuan, B.; Chen, V.; Li, H.; Hui, F.; Yu, Z.; Yuan, F.; Pop, E.; Wong, H.-S. P.; Lanza, M. Electronic Synapses Made of Layered Two-Dimensional Materials. *Nat. Electron.* **2018**, *1*, 458−465.

DOI: 10.1021/acsami.9b13434
ACS Appl. Mater. Interfaces 2019, 11, 43473−43479